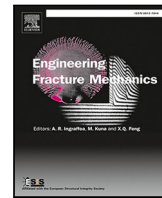




ELSEVIER

Contents lists available at ScienceDirect

Engineering Fracture Mechanics

journal homepage: www.elsevier.com/locate/engfracmech

Phase field formulation for the fracture of a metal under impact with a fluid formulation

Shourong Hao^a, Yongxing Shen^{a,b,*}, Jun-Bo Cheng^c^a University of Michigan – Shanghai Jiao Tong University Joint Institute, Shanghai Jiao Tong University, Shanghai, 200240, China^b Shanghai Key Laboratory for Digital Maintenance of Buildings and Infrastructure, Shanghai 200240, China^c Laboratory of Computational Physics, Institute of Applied Physics and Computational Mathematics, Beijing 100094, China

ARTICLE INFO

Keywords:

Impact
Phase field model
Finite deformation
Updated Lagrangian framework
Mie–Grüneisen equation of state
Hydrodynamic code

ABSTRACT

This work is concerned with the impact problems of metals involving intense shock waves. To account for different fracture modes, we develop a phase field model with new formulation of the thermodynamic driving force. This driving force is based on a new history variable dependent on two critical energy release rates, one for volumetric loading and the other for shear loading. The formulation is based on an updated Lagrangian framework. In contrast to most existing phase field models, usually implemented under total Lagrangian framework, we have adopted an equation of state for pressure, and artificial viscosity to deal with the strong shock waves. Besides, the hypoelastic elastoplastic constitutive model and the Johnson–Cook model are adopted to consider the strain hardening, strain rate hardening, and thermal softening at finite deformation, high temperature, and high strain rate situations. Another feature of the proposed model compared with existing models is that the former needs two or three fewer parameters. The proposed model is validated by experimental results. Moreover, parametric studies on the impact velocity and the Taylor–Quinney coefficient are conducted, which shows that different fracture modes can be captured, and the Taylor–Quinney coefficient has a significant effect on the results. Besides, global sensitivity analysis is performed to study the effect of a few key parameters on the fracture characteristics.

1. Introduction

Dynamic impact problems of metals, e.g., explosions and projectile impacts, are an important class of problems in engineering. The theory and physical behavior of impact was explained in detail by Goldsmith [1]. The impact problems with strong shock waves are usually simulated with hydrocodes, in which the metal is treated as a fluid as opposed to a solid.

There are numerical methods for the fracture simulations of impact problems, e.g., the cohesive zone model by Camacho et al. [2], the continuum damage model by Børvik et al. [3], the distinct element method by Thornton et al. [4], the mesh-free Galerkin method by Li et al. [5,6], Rabczuk and Belytschko [7,8], peridynamics by Ren et al. [9], and so on.

The recently developed phase field models also provide a promising strategy to handle the fracture of impact. The phase field approach [10] is a regularization of the variational theory of fracture proposed by Francfort and Marigo [11]. One key advantage compared with the traditional fracture methods is that phase field models do not need to track the crack paths, and the cracks nucleate, propagate, branch, and merge naturally without any extra criterion. For more detailed descriptions of phase field models, the reader is referred to the reviews by Ambati et al. [12], Wu et al. [13], Bourdin and Francfort [14], and Francfort [15].

* Corresponding author at: University of Michigan – Shanghai Jiao Tong University Joint Institute, Shanghai Jiao Tong University, Shanghai, 200240, China.
E-mail address: yongxing.shen@sjtu.edu.cn (Y. Shen).

There have been phase field models to simulate dynamic fracture. In terms of the kinematic representation, these models can be classified into three categories: small deformation models, “hyperelastic” models, and “hypoelastic” models. Under small deformation, Nguyen and Wu [16] applied their static phase field cohesive zone model [17] to the dynamic cases for brittle and quasi-brittle materials. A feature of this model is that the result is independent from the regularization length scale. Zhou et al. [18] realized dynamic crack propagation in infinitesimal deformation for brittle materials by COMSOL, and they also studied the effect of the mesh size, time step, energy release rate, and so on, on phase field. Ren et al. [19] developed an explicit phase field model for dynamic fracture in brittle materials. In their model, the displacement field is updated with a velocity Verlet scheme, and the phase field is integrated with an adaptive sub-step strategy. Mandal et al. [20] evaluated several phase field models for dynamic brittle fracture through studying the mesh dependency, length scale sensitivity, branching angle, crack tip position/velocity, and so on. Zhang et al. [21] extended the phase field cohesive zone model to simulate spall fracture, and investigated three types of traction–separation laws for softening and different parameters in detail.

Based on the “hyperelastic” model, i.e., a multiplicative decomposition of the deformation gradient into elastic and plastic parts, Miehe et al. [22] employed the phase field model to investigate ductile fracture at finite strains. They proposed energetic and stress-based forces for fracture, which considered the inelastic response by the state variables, such as the amount of plastic strain and void volume fraction. McAuliffe and Waismann [23,24] developed a coupled thermo-visco-plasticity phase field model under finite deformation, in which they treated part of plastic work as one source of fracture energy available for crack propagation. Borden et al. [25] introduced a plasticity softening mechanism by the yield surface degradation function in the phase field model, together with a mechanism considering the stress triaxiality as a driving force for fracture. Ambati et al. [26] proposed a phase field model in finite deformation for ductile materials, with a relation between the degradation function and a scalar value associated with the accumulated plastic strain.

Along the line of “hypoelastic” models, i.e., an additive decomposition of elastic and plastic strain rates, Chu et al. [27] proposed a dynamic phase field model in which the critical fracture energy release rate varies with the stress triaxiality to distinguish tension and shear. Employing the Johnson–Cook model to consider the strain hardening, strain rate hardening and thermal softening, Wang et al. [28,29] developed a unified phase field model to study the shear band phenomena under impact loading. Zhang et al. [30] proposed a phase field model for adiabatic shear bands in thick-walled-cylinders, where an energetic degradation function and a crack geometric function are adopted. There are different opinions on hypoelastic models in general [31, Chapter 9] and in this context [32]; nevertheless, a numerical comparison by Brepols et al. [33] shows that the two models provide nearly the same results, which suggests that both are suitable for elastoplastic materials.

The phase field model for fracture can be formulated as an elliptic equation with a thermodynamic driving force as the source term. The formulation of this driving force is a critical issue. There are many different choices of driving forces. The starting point to write down the driving force is to write it as the negative of the derivative of free energy density with respect to the phase field variable. This already leads to a multitude of expressions as many variants of the strain energy density functions exist to take into account the unilateral constraint of the crack faces, see [10,34–37]. Besides, in order to avoid crack healing, certain ingredient must be present in the formulation. One such option is introduced by Miehe et al. [38], in which the historically maximum value of the said functional derivative is taken as the driving force, as opposed to the functional derivative itself.

Compared with solid codes, hydrocodes may be more attractive to handle the highly dynamic situations with intense shock waves. More details of hydrocodes can be found in Benson [39] and Zukas [40]. The aforementioned Ref. [21] is based on a hydrodynamic code.

In this paper, we propose a phase field model for impact problems based on the hypoelastic elastoplasticity model under finite deformation. We adopt the Johnson–Cook constitutive model to consider the strain hardening, strain rate hardening and thermal softening, and von Mises yield criterion for plastic flow. We employ the Mie–Grüneisen equation of state to relate pressure, density and internal energy density under high temperature and pressure.

As for the implementation, the entire framework is based on the updated Lagrangian scheme and implemented by a hydrodynamic code. The phase field governing equation, which is stated in the deformed configuration, appears differently from most existing models, as the latter are often stated in the undeformed configuration. In the hydrodynamic code, the deviatoric stress and pressure are updated separately, with the displacement solution obtained by explicit integration. In order to capture intense shock waves accurately, some extra formulations are augmented, such as artificial viscosity.

The driving force is also newly formulated, to take into account the effects of volumetric and shear loads. This driving force is the energy available for crack propagation in the form of phase field evolution, which plays a central role in the proposed model. This driving force is written in terms of a novel history variable, which is developed to distinguish the different effects of tension and compression, with different treatments of the elastic and plastic stored energies. The key point here is that there is no artificial parameters, which also distinguishes the proposed model with most of the existing models, such as Miehe et al. [22] and Chu et al. [27]. With these at hand, the driving force is reformulated about the proposed history variable with different energy release rates for volumetric and shear loading, which is in stark contrast to the existing models.

The paper is organized as follows. In Section 2, the whole model is proposed, including kinematics, equation of state, artificial viscosity, hourglass viscosity, elastic, and plastic constitutive model, and the phase field model. The discretizations in both space and time are discussed in Section 3, and the detailed update scheme is summarized. Then in Section 4, the proposed model is validated with experimental results in the literature, and the effects of the phase field regularization parameter, critical energy release rates for volumetric loading and shear loading, and the Taylor–Quinney coefficient are studied. Finally, conclusions are given in Section 5.

2. Formulations

In this section, the key governing equations of elastoplastic under impact are summarized. First, the basic kinematic and conservation equations are reviewed. Then, the Mie–Grüneisen equation of state and the elastic and plastic constitutive models will be presented in detail, and the volumetric–deviatoric decomposition of stress is adopted throughout the text. Finally, a novel phase field model with the ability to handle both tensile and shear fractures will be elaborated for impact fracture simulations.

2.1. Kinematics and conservation equations

Consider an elastoplastic fluid. Let \mathbf{X} represent the particle position in the reference configuration, and $\mathbf{x} = (x, y)$ represent the corresponding particle position in the current configuration at time t , and the deformation mapping is $\mathbf{x} = \varphi(\mathbf{X}, t)$. Then the deformation gradient \mathbf{F} is

$$\mathbf{F} = \frac{\partial \mathbf{x}}{\partial \mathbf{X}} = \frac{\partial \varphi(\mathbf{X}, t)}{\partial \mathbf{X}}, \quad (1)$$

and the Jacobian $J = \det(\mathbf{F})$.

The left Cauchy–Green strain tensor \mathbf{b} is defined as¹

$$\mathbf{b} = \mathbf{F}\mathbf{F}^T. \quad (2)$$

Let $\mathbf{v} = d\mathbf{x}/dt$ be the fluid velocity, then the spatial velocity gradient \mathbf{L} is defined as

$$\mathbf{L} = \nabla \mathbf{v} = \dot{\mathbf{F}}\mathbf{F}^{-1} = \mathbf{D} + \mathbf{W}, \quad (3)$$

where by definition the gradient is taken with respect to the current coordinate \mathbf{x} , $\mathbf{D} = (1/2)[\nabla \mathbf{v} + (\nabla \mathbf{v})^T]$ is the rate of deformation tensor, and $\mathbf{W} = (1/2)[\nabla \mathbf{v} - (\nabla \mathbf{v})^T]$ is the spin tensor, also called the vorticity tensor.

The rate of deformation tensor \mathbf{D} is additively decomposed as

$$\mathbf{D} = \mathbf{D}^e + \mathbf{D}^p, \quad (4)$$

where \mathbf{D}^e and \mathbf{D}^p are the elastic and plastic parts of the deformation rate, respectively. The elastic part \mathbf{D}^e is further decomposed into the volumetric part and the deviatoric part, the latter of which reads

$$\mathbf{D}_{\text{dev}}^e = \mathbf{D}^e - \frac{1}{3} \text{tr}(\mathbf{D}^e) \mathbf{I}.$$

The governing equations of Lagrangian fluid mechanics developed by Wilkins [41] are given below:

- Conservation of mass (equation of continuity):

$$\frac{D\rho}{Dt} + \rho \nabla \cdot \mathbf{v} = 0, \quad (5)$$

where ρ is the current density.

- Conservation of momentum, with body force neglected:

$$\rho \mathbf{a} = \nabla \cdot \boldsymbol{\sigma} = -\nabla p + \nabla \cdot \mathbf{s}, \quad (6)$$

where $\mathbf{a} = D\mathbf{v}/Dt$ is the acceleration field, $\boldsymbol{\sigma}$ is the Cauchy stress tensor, $p = -(1/3)\text{tr}(\boldsymbol{\sigma})$ is the hydrostatic pressure, and $\mathbf{s} = \boldsymbol{\sigma} + p\mathbf{I}$ is the stress deviator.

- Balance of internal energy. To introduce the balance of internal energy, we first examine the energies involved: the volumetric strain energy density ψ^{vol} , the elastic distortional energy density $\psi^{e,\text{dev}}$, and the energy density corresponding to plastic work ψ^p . For convenient use in the hypoelastic formulation which will be talked later, the energy densities are listed below in a rate form:

$$\dot{\psi}^{\text{vol}} = -p \text{tr}(\mathbf{D}), \quad \dot{\psi}^{e,\text{dev}} = \mathbf{s} : \mathbf{D}_{\text{dev}}^e, \quad \dot{\psi}^p = \mathbf{s} : \mathbf{D}^p. \quad (7)$$

With these, the balance of internal energy reads

$$\rho \frac{De}{Dt} = \dot{\psi}^{\text{vol}} + \dot{\psi}^{e,\text{dev}} + \chi \dot{\psi}^p, \quad (8)$$

where e is the internal energy per unit mass, χ is the Taylor–Quinney fraction that represents the fraction of the inelastic work converted to heat.

¹ Some authors use a dot, like $\mathbf{F} \cdot \mathbf{F}^T$, in such expression involving the single contraction of two tensors. Here we adopt the convention that such dot is omitted unless necessary to avoid ambiguity.

2.2. The equation of state

An equation of state is needed for the compressible fluid. For concreteness, the Mie–Grüneisen equation of state with cubic shock velocity–particle velocity [42] is adopted in this work to describe the metal behavior under high temperature and high pressure, while many other equations of state can also be used.

When the material is damaged but not fully broken, it can still undergo compression like in the intact state, but the ability to endure tension becomes weaker. Later we will introduce the phase field d to describe such damage. In particular, we degrade the hydrostatic pressure as

$$p = \begin{cases} p_{\text{MG}}, & \mu \geq 0, \\ g(d)p_{\text{MG}}, & \mu < 0, \end{cases} \quad (9)$$

where $\mu = \rho/\rho_0 - 1$ with ρ_0 the initial density, the degradation function $g(d)$ is defined in (24), and the pressure p_{MG} is calculated from

$$p_{\text{MG}} = \begin{cases} \frac{\rho_0 \mu C_{\text{MG}}^2 [1 + (1 - \gamma_0/2) \mu]}{[1 - (S_1 - 1) \mu]^2} + \gamma_0 \rho_0 e, & \mu \geq 0, \\ \rho_0 \mu C_{\text{MG}}^2 + \gamma_0 \rho_0 e, & \mu < 0, \end{cases} \quad (10)$$

where C_{MG} is the bulk speed of sound, which is the y -intercept of the U_s – U_p curve, also known as the Hugoniot curve, where U_s is the shock wave speed, U_p is the particle velocity; S_1 is the slope of the U_s – U_p curve, and γ_0 is Grüneisen's gamma parameter at the reference state.

2.3. Elastoplastic constitutive model

This subsection presents a coupled hypoelastic and J_2 plastic constitutive model, with the Johnson–Cook model adopted for modeling strain hardening, strain rate hardening, and thermal softening.

Hypoelastic–plastic constitutive model. With the hypoelastic–plastic constitutive model adopted, and the additive decomposition of the rate of deformation (4), we adopt the Jaumann stress rate for s for objectivity:

$$\overset{\nabla}{s} = \frac{D s}{D t} + s \mathbf{W} - \mathbf{W} s. \quad (11)$$

An objective elastic constitutive response is given by

$$\overset{\nabla}{s} = 2G \mathbf{D}_{\text{dev}}^e, \quad (12)$$

where $G > 0$ is the shear modulus.

Johnson–cook constitutive model with degradation. In this work, the Johnson–Cook constitutive model [43] is adopted, as it provides an adequate description of the materials subjected to finite strain, high strain rate, and high temperature. It is noted that other constitutive models such as ideal elastoplasticity and the Steinberg–Guinan model [44] can also be employed. In the Johnson–Cook model, the yield stress is expressed as

$$\sigma_y^0 = [A + B \epsilon^n] \left[1 + C \ln \frac{\dot{\epsilon}}{\dot{\epsilon}_0} \right] \left[1 - \left(\frac{T - T_0}{T_m - T_0} \right)^m \right], \quad (13)$$

where ϵ is the equivalent plastic strain, whose rate of change is given by

$$\dot{\epsilon} = \sqrt{\frac{2}{3} \mathbf{D}^p : \mathbf{D}^p},$$

T is the absolute temperature, A , B , C , n , and m are material properties, $\dot{\epsilon}_0$ is a reference plastic strain rate, T_0 is the reference temperature, and T_m is the melt temperature.

In order to consider the effect of damage on the materials, the yield stress is degraded such that the effective yield stress is expressed as

$$\sigma_y = g(d) \sigma_y^0, \quad (14)$$

where the degradation function $g(d)$ is defined in (24).

The temperature field and the J_2 flow rule will be elaborated below.

Evolution of temperature. In the assumption of adiabatic condition and negligible heat conduction, the local rate of change of temperature can be expressed as

$$\rho C_v \frac{DT}{Dt} = \chi \psi^p, \quad (15)$$

where C_v is the specific heat capacity at constant volume.

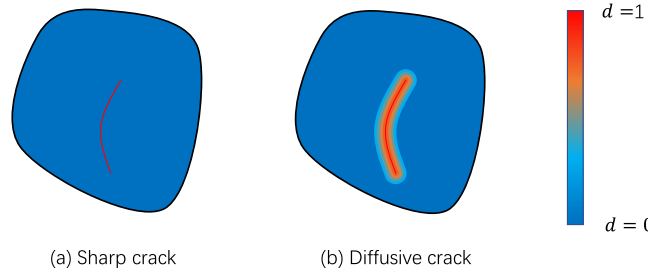


Fig. 1. Comparison of a traditional sharp-crack description and a diffusive-crack description as in the phase field approach.

J₂ Flow rule. For the yield condition given in (13), we adopt the von Mises yield criterion. The yield function is expressed as

$$f(s, \epsilon, \dot{\epsilon}, T, d) = \bar{\sigma} - \sigma_y, \quad (16)$$

where $\bar{\sigma} = \sqrt{\frac{3}{2}s : s}$ is the effective stress.

The plastic flow rule and evolution equation are stated as

$$\mathbf{D}^p = \gamma \frac{3s}{2\bar{\sigma}}, \quad \gamma = \dot{\epsilon}, \quad (17)$$

where γ is the plastic consistency parameter.

Finally, the loading-unloading conditions are

$$\gamma \geq 0, \quad f \leq 0, \quad \gamma f = 0, \quad (18)$$

and the persistency condition is

$$\gamma f = 0. \quad (19)$$

2.4. The phase field model for fracture

This section develops the phase field model for fracture for an elastoplastic fluid. The main novelty is to express the driving-force as the contribution from a new history variable to consider the different fracture mechanisms of tension and shear fractures. The actual equation used is given as (25).

In a nutshell, the phase field model introduces a diffusive field d with a range of $[0, 1]$ to represent the state of material, where $d = 0$ and $d = 1$ represent the pristine and fully broken states, respectively, shown as Fig. 1.

Governing equation in the reference configuration. Following Miehe et al. [38], the governing equation for the phase field d in the reference configuration will be written as an elliptic equation, with the source term being the *driving force* as

$$\frac{1}{\ell} (d - \ell^2 \nabla_X^2 d) = 2(1-d) \frac{\mathcal{H}}{g_c}, \quad (20)$$

where g_c is the critical energy release rate, $\ell > 0$ is the regularization parameter, and \mathcal{H} is a certain variable to take into account the irreversibility, typically the historically maximum value of a certain part of the free energy density.

In the proposed model, the governing equation in the reference configuration is

$$\frac{1}{\ell} (d - \ell^2 \nabla_X^2 d) = 2(1-d) \mathcal{H}, \quad (21)$$

where the driving force on the right hand side consists of a volumetric term and a deviatoric term, associated with the respective parts of the elastoplastic energy, Heav is the Heaviside function, ensuring only under tension is the volumetric part degraded, g_c^{vol} and g_c^{dev} are the critical energy release rates for tension and shear fractures, respectively, and a new history variable is introduced to account for the irreversibility, which is defined as

$$\mathcal{H} = \max_{[0,t]} \left\{ \text{Heav}(-\mu) \frac{\psi_0^{\text{vol}}}{g_c^{\text{vol}}} + \frac{\psi_0^{\text{e.dev}} + (1-\chi)\psi^p}{g_c^{\text{dev}}} \right\}. \quad (22)$$

where ψ_0^{vol} and $\psi_0^{\text{e.dev}}$ are the undegraded volumetric strain energy density and the undegraded elastic distortional strain energy density, respectively.

The rate of undegraded volumetric strain energy density $\dot{\psi}_0^{\text{vol}}$ and of undegraded elastic distortional strain energy density $\dot{\psi}_0^{\text{e.dev}}$ are determined as

$$\dot{\psi}_0^{\text{vol}} = \begin{cases} \dot{\psi}^{\text{vol}} / g(d), & \mu < 0, \\ \dot{\psi}^{\text{vol}}, & \mu \geq 0, \end{cases} \quad \dot{\psi}_0^{\text{e.dev}} = \frac{\dot{\psi}^{\text{e.dev}}}{g(d)}, \quad (23)$$

where the degradation function $g(d)$ is given by

$$g(d) = (1 - d)^2 + \eta, \quad (24)$$

with η a very small number for the stability of computation, e.g., 10^{-10} .

Remark. Compared with the existing models proposed by Miehe et al. [22] and Chu et al. [27], there is no artificial parameters which may affect the results in our model, e.g., the slope parameter δ , the strain rate transition $\dot{\epsilon}_{\text{trans}}$, and the critical equivalent plastic strain α_{crit} in the model of Miehe et al. [22], and the energy threshold for tensile fracture w_{0T} and for shear banding w_{0S} , the critical stress triaxiality η_{cr} , and the transitional parameter δ in the model of Chu et al. [27]. Besides, our proposed model is concise and computationally efficient, and has fewer parameters needed compared with the existing models.

Remark. A remark on $g(d)$ appearing in the denominators in (23) follows. Recall that the yield stress is degraded in (14), effectively the Cauchy stress σ is also degraded as the magnitude of s is bounded by σ_y . The presence of $g(d)$ in (23) is used to recover the energy to the undegraded state, to be consistent with the phase field fracture literature.

Governing equation in the current configuration. Since our phase field model is referenced to the current domain, the governing equation becomes

$$\frac{1}{\ell} [d - J\ell^2 \nabla \cdot (J^{-1} b \nabla d)] = 2(1 - d)\mathcal{H}. \quad (25)$$

The corresponding boundary condition is

$$n \cdot b \nabla d = 0$$

on the external boundary, where ∇ , again, represents the gradient operator associated with the current domain.

3. Discretization and numerical algorithms

In this section, we elaborate the discretization of the governing equations, and the adopted algorithms for numerical solution.

First we will discretize in both time and space, and recapitulate the artificial viscosity and hourglass viscosity under the case of a quadrilateral mesh in two dimensions, then we give the weak forms of displacement and phase field and the corresponding discretization. At last, we discretize the energy equation and state the return mapping algorithm.

Overall speaking, for the impact problems, the displacement is solved explicitly by the central difference method, in which the nodal forces are computed with reduced integration, and the phase field is solved implicitly with full integration. Within the implicit solver, we adopt the restarted generalized minimal residual (GMRES) solver preconditioned by incomplete LU decomposition (ILU) to solve the linear system resulting from the Newton–Raphson iteration. Besides, we employ the OpenMP multi-threaded parallelism technique to accelerate the for-loop calculations.

In terms of data organization, the velocity, acceleration, position, displacement, hourglass viscosity, and the phase field variable are stored at the nodes, and the rate of deformation, stress, pressure, artificial viscosity, temperature, equivalent plastic strain and its rate, and history variable are stored at the Gauss points. The whole updating process is shown in Algorithm 1.

3.1. Spatial and temporal discretizations

For the discretization in time domain, we use the standard central difference method with varying time step sizes [42]. Firstly, we define the time increment as, for $k \in \mathbb{N}$,

$$\Delta t^k = t^{k+1} - t^k, \quad \Delta t^{k+1/2} = \frac{1}{2} (\Delta t^k + \Delta t^{k+1}), \quad (26)$$

where Δt^k is the time step size, which is determined by the Courant number, a scalar that renders the time integration stable, which depends on the sound speed, characteristic length of meshes, density, and the artificial viscosity coefficients, see [42, Equation (22.2)].

The initial domain Ω_0 is discretized by a mesh with quadrilateral elements and the displacement and phase field are discretized by

$$\mathbf{u}(\mathbf{x}) = \sum_{a=1}^4 N_a^k(\mathbf{x}) \mathbf{u}_a, \quad d(\mathbf{x}) = \sum_{a=1}^4 N_a^k(\mathbf{x}) d_a, \quad (27)$$

where \mathbf{u}_a and d_a are the displacement and phase field values, respectively, of node a , and $N_a^k(\mathbf{x})$ is the standard finite element shape function at the k th step. Once the solution is obtained, the nodes move according to their nodal displacements, forming the mesh for Ω_1 , and so on for Ω_k . For notational simplicity, the step number k is not marked in \mathbf{u} and d appearing in (27).

3.2. Artificial and hourglass viscosities

Here, we recapitulate two standard setups in a hydrocode, namely the artificial viscosity to alleviate the discontinuity generated by the shock waves, and the hourglass viscosity to suppress the hourglass modes caused by reduced integration.

Algorithm 1: The whole updating procedure of the key variables from time step t^k to t^{k+1}

Input: $\mathbf{x}^k, \mathbf{v}^{k-1/2}, \mathbf{a}^k, \mathbf{d}^k, \Delta t^k, \Delta t^{k+1/2}, \mathbf{M}, \text{tol}$
Output: $\mathbf{x}^{k+1}, \mathbf{v}^{k+1/2}, \mathbf{a}^{k+1}, \mathbf{d}^{k+1}$
// Kinematic updating

 Update the velocity by $\mathbf{v}^{k+1/2} = \mathbf{v}^{k-1/2} + \Delta t^k \mathbf{a}^k$;

 Calculate the displacement at the current step by $\mathbf{u}^{k+1} = \Delta t^{k+1/2} \mathbf{v}^{k+1/2}$;

// Deformation, hourglass viscosity, and temperature updating

 Calculate rate of deformation \mathbf{D} and spin tensor \mathbf{W} by (3);

 Calculate hourglass viscosity f_{ia}^h by (32);

 Update temperature T by (15);

// Constitutive model updating

 Calculate yield stress by Johnson–Cook model σ_y^0 by (13);

 Calculate the degraded yield stress σ_y by (14) and the trial stress s_{ij}^{trial} by (43);

 Calculate the stress deviator s_{ij}^{k+1} by radial return mapping algorithm (44);

 Calculate the plastic rate of deformation \mathbf{D}^p by (45);

// Pressure, artificial viscosity, and energy updating

Calculate the first term of equation of state (10);

 Calculate artificial viscosity q by (28);

 Calculate the internal energy at half step $e^{k+1/2}$ by (40);

 Calculate the second term of equation of state and update the pressure p_{MG} by (10);

 Calculate the degraded pressure p under tension ($\mu < 0$) by (9);

 Calculate the internal energy at the end of the time step e^{k+1} by (41);

// Displacement and acceleration updating

 Calculate and assemble nodal residual force \mathbf{R}_A by (35);

 Calculate acceleration by $\mathbf{a}^{k+1} = -\mathbf{M}^{-1} \mathbf{R}_d(\mathbf{u}^{k+1}, \mathbf{d}^k)$;

 Update position by $\mathbf{x}^{k+1} = \mathbf{x}^k + \mathbf{u}^{k+1}$;

// Phase field solving

 Find \mathbf{d}^{k+1} such that $\|\mathbf{R}_d(\mathbf{d}^{k+1}; \mathbf{x}^{k+1}, \mathbf{x}^0, p^{k+1}, s^{k+1}, \mathbf{D}^{k+1})\| < \text{tol}$ by Newton–Raphson iteration, where the inner linear equations are solved by preconditioned GMRES;

3.2.1. The artificial viscosity

In order to smear the discontinuity appearing in shock waves into continuous but rapidly varying region, Von Neumann and Richtmyer [45] proposed to add a viscous term q into the pressure term [42].

For a given quadrilateral element, the expression for q for each element is

$$q = \begin{cases} \rho \Delta x \text{tr}(\mathbf{D}) (b_1 c - b_2 \Delta x \text{tr}(\mathbf{D})) , & \text{tr}(\mathbf{D}) < 0, \\ 0, & \text{tr}(\mathbf{D}) \geq 0, \end{cases} \quad (28)$$

where c is the sound speed, $\Delta x = \sqrt{2A}/\sqrt{\max(d_{24}^2, d_{13}^2)}$ is the characteristic length scale of the element, with A the area of the element, and d_{24} and d_{13} the lengths of the two diagonals.

Then the conservation of momentum (6) becomes

$$\rho \mathbf{a} = \nabla \cdot (\boldsymbol{\sigma} - q \mathbf{I}), \quad \text{in each element,}$$

where \mathbf{I} is the identity tensor, while the balance of internal energy (8) reads

$$\rho \frac{D e}{D t} = \dot{\psi}^{\text{e,dev}} + \chi \dot{\psi}^p - (p + q) \text{tr}(\mathbf{D}). \quad (29)$$

3.2.2. The hourglass viscosity

In order to reduce the computational cost, a single integration point is adopted for each quadrilateral element for the updating of displacement field, which may cause hourglass deformation. Flanagan and Belytschko [46] overcame this problem by adding an hourglass viscosity term.

Firstly, for each element, \dot{q}_i^h is defined as

$$\dot{q}_i^h = \sum_{a=1}^4 \Gamma_a v_{ia}, \quad (30)$$

where $i = x, y$ represent the Cartesian directions, a is the local node number of the element of interest in the counterclockwise order, $(\Gamma_1, \Gamma_2, \Gamma_3, \Gamma_4) = (1, -1, 1, -1)$, and v_{ia} is the velocity of node a . Then the default hourglass viscosity is

$$Q_i^h = \frac{1}{4} \varepsilon \rho c \sqrt{A} \dot{q}_i^h, \quad (31)$$

where ε is an hourglass parameter, and c is the sound speed. The resultant hourglass viscosity force is expressed as

$$f_{ia}^h = Q_i^h \Gamma_a. \quad (32)$$

Finally, the conservation of momentum becomes

$$\rho \mathbf{a} = \nabla \cdot (\sigma - q \mathbf{I}) + \mathbf{f}^h, \quad \text{in each element.} \quad (33)$$

3.3. Weak forms and discretization

Here we provide the weak forms for the conservation of momentum (33) and the governing equation of phase field (25).

For the displacement. For the k th time step, define the set of admissible displacement fields $\mathbb{V}_k = \{\mathbf{u}(\cdot, t) \in H^1(\Omega_k; \mathbb{R}^n) | \mathbf{u} = \mathbf{u}_D \text{ on } \partial_D \Omega_k\}$. Then the weak form for the displacement at t_k corresponding to (33) is: Find $\mathbf{u}(t) \in \mathbb{V}_k$ such that

$$\int_{\Omega_k} \bar{\mathbf{u}} \cdot \rho \mathbf{a} \, d\Omega + \int_{\Omega_k} [\sigma(\mathbf{u}) - q \mathbf{I}] : \epsilon(\bar{\mathbf{u}}) \, d\Omega = \int_{\Omega_k} \bar{\mathbf{u}} \cdot \mathbf{f}^h \, d\Omega + \int_{\partial_N \Omega_k} \bar{\mathbf{u}} \cdot \mathbf{t} \, d\Gamma, \quad \forall \bar{\mathbf{u}} \in \mathbb{Z}_k, \quad (34)$$

where $\mathbb{Z}_k = \{\bar{\mathbf{u}} \in H^1(\Omega_k; \mathbb{R}^n) | \bar{\mathbf{u}} = 0 \text{ on } \partial_D \Omega_k\}$, \mathbf{t} is the traction, and

$$\epsilon(\bar{\mathbf{u}}) = \frac{1}{2} \left[\nabla_k \bar{\mathbf{u}} + (\nabla_k \bar{\mathbf{u}})^T \right],$$

where ∇_k represents the gradient with respect to the spatial coordinates at the k th time step.

By the weak form of displacement (34), the residual vector \mathbf{r}_u^Q of displacement for element Q is given by

$$\mathbf{r}_u^Q = \int_{\Omega_k} (\hat{\mathbf{B}}_Q^k)^T [\sigma(\mathbf{u}) - q \mathbf{I}] \, d\Omega - \int_{\Omega_k} (\hat{\mathbf{N}}_Q^k)^T \mathbf{f}^h \, d\Omega - \int_{\partial_N \Omega_k} (\hat{\mathbf{N}}_Q^k)^T \mathbf{t} \, d\Gamma, \quad (35)$$

where we adopt Voigt notion for tensor for simplicity, and $\hat{\mathbf{B}}_Q^k$ and $\hat{\mathbf{N}}_Q^k$ are the strain-displacement matrix and shape function matrix, respectively.

$$\begin{aligned} \hat{\mathbf{N}}_Q^k &= \begin{bmatrix} N_1^k & 0 & \dots & N_4^k & 0 \\ 0 & N_1^k & \dots & 0 & N_4^k \end{bmatrix}, \\ \hat{\mathbf{B}}_Q^k &= \begin{bmatrix} \partial N_1^k / \partial x & 0 & \dots & \partial N_4^k / \partial x & 0 \\ 0 & \partial N_1^k / \partial y & \dots & 0 & \partial N_4^k / \partial y \\ \partial N_1^k / \partial y & \partial N_1^k / \partial x & \dots & \partial N_4^k / \partial y & \partial N_4^k / \partial x \end{bmatrix}. \end{aligned}$$

For the phase field. The weak form for the phase field equation corresponding to (25) is: Find $d \in H^1(\Omega_k) \cap L^\infty(\Omega_k)$ such that

$$\int_{\Omega_k} g'(d) \mathcal{H} \frac{\bar{d}}{J_k} \, d\Omega + \int_{\Omega_k} \left(\frac{d\bar{d}}{\ell} + \ell (\nabla_k d)^T \mathbf{b}_k \nabla_k \bar{d} \right) \frac{1}{J_k} \, d\Omega = 0, \quad \forall \bar{d} \in H^1(\Omega_k) \cap L^\infty(\Omega_k), \quad (36)$$

where J_k and \mathbf{b}_k are the Jacobian and the left Cauchy-Green tensor, both relative to the initial configuration at k th time step.

By the weak form of phase field (36), we obtain the elemental residual vector for element Q \mathbf{r}_d^Q and tangent stiffness matrix \mathbf{k}_d^Q as follows:

$$\begin{aligned} \mathbf{r}_d^Q &= \int_{\Omega_k^Q} g'(d) \mathcal{H} J_k^{-1} (\mathbf{N}_Q^k)^T \, d\Omega + \frac{1}{\ell} \int_{\Omega_k^Q} d J_k^{-1} (\mathbf{N}_Q^k)^T \, d\Omega \\ &\quad + \ell \int_{\Omega_k^Q} J_k^{-1} (\nabla_k \mathbf{N}_Q^k)^T \mathbf{b}_k \nabla_k d \, d\Omega, \end{aligned} \quad (37)$$

$$\begin{aligned} \mathbf{k}_d^Q &= \int_{\Omega_k^Q} g''(d) \mathcal{H} J_k^{-1} (\mathbf{N}_Q^k)^T \mathbf{N}_Q^k \, d\Omega + \frac{1}{\ell} \int_{\Omega_k^Q} J_k^{-1} (\mathbf{N}_Q^k)^T \mathbf{N}_Q^k \, d\Omega \\ &\quad + \ell \int_{\Omega_k^Q} J_k^{-1} (\nabla_k \mathbf{N}_Q^k)^T \mathbf{b}_k \nabla_k \mathbf{N}_Q^k \, d\Omega, \end{aligned} \quad (38)$$

where the shape function \mathbf{N}_Q^k and the corresponding derivatives $\nabla_k \mathbf{N}_Q^k$ are

$$\mathbf{N}_Q^k = [N_1^k, \dots, N_4^k], \quad \nabla_k \mathbf{N}_Q^k = \begin{bmatrix} \partial N_1^k / \partial x & \dots & \partial N_4^k / \partial x \\ \partial N_1^k / \partial y & \dots & \partial N_4^k / \partial y \end{bmatrix}.$$

After acquiring \mathbf{r}_u^Q , \mathbf{r}_d^Q and \mathbf{k}_d^Q , we obtain the global residual vector \mathbf{R}_u , \mathbf{R}_d and stiffness matrix \mathbf{K}_d by the standard assemble procedure of the Galerkin finite element method.

3.4. The discretization for the energy equation

We discretize the conservation of energy (29) by the finite volume method, and the internal energy per unit mass e is discretized as

$$m_Q \frac{e^{k+1} - e^k}{\Delta t^k} = - \left(\frac{p^k + p^{k+1}}{2} + q^k \right) \left(\frac{\Delta V_Q^{k+1}}{\Delta t^k} \right) + w_s, \quad (39)$$

where $m_Q = \rho_0^Q V_0^Q$ is the mass of element Q , and

$$w_s = V_Q^{k+1/2} s_{ij}^{k+1/2} \left(D_{ij}^{e,k+1/2} + \chi D_{ij}^{p,k+1/2} \right), \quad \Delta V_Q^{k+1} = V_Q^{k+1} - V_Q^k,$$

and V_Q^k is the volume of element Q at the k th time step.

In practice, we update e in two separate steps:

$$m_Q (e^{k+1/2} - e^k) = - \left(\frac{p^k}{2} + q^k \right) \Delta V_Q^{k+1} + \Delta t^k w_s, \quad (40)$$

$$m_Q (e^{k+1} - e^{k+1/2}) = - \frac{p^{k+1}}{2} \Delta V_Q^{k+1}. \quad (41)$$

3.5. The return mapping algorithm

The return mapping algorithm is adopted to update the stress given the total strain increment. This consists of a predictor step and a corrector step.

Firstly, we define the rotational term in (11) as

$$R_{ij} = s_{ip} W_{pj} - W_{ip} s_{pj} = s_{ip} \left[\frac{1}{2} \left(\frac{\partial v_p}{\partial x_j} - \frac{\partial v_j}{\partial x_p} \right) \right] + s_{pj} \left[\frac{1}{2} \left(\frac{\partial v_p}{\partial x_i} - \frac{\partial v_i}{\partial x_p} \right) \right]. \quad (42)$$

Then by the finite difference method, the trial deviatoric stress is written as

$$s_{ij}^{\text{trial}} = s_{ij}^k + \Delta t^k \left(2G D_{ij}^{\text{dev}} - \bar{R}_{ij} \right) \quad (43)$$

where G is the shear modulus, and

$$D_{ij}^{\text{dev}} = D_{ij} - \frac{1}{3} D_{mm} \delta_{ij}, \quad \bar{R}_{ij} = \frac{1}{A_k} \int_{\Omega_k^Q} R_{ij} dA,$$

and A_k is the area of the element Q in k th time step.

The corrected deviatoric stress at the next time step is

$$s_{ij}^{k+1} = s_{ij}^{\text{trial}} \min \left\{ 1, \frac{\sigma_y}{\bar{\sigma}_0^{\text{trial}}} \right\}, \quad (44)$$

where $\bar{\sigma}_0^{\text{trial}} = \sqrt{\frac{3}{2} s_{ij}^{\text{trial}} s_{ij}^{\text{trial}}}$, and the corrected plastic part of the rate of deformation \mathbf{D}^p is

$$\mathbf{D}^p = \frac{s_{ij}^{\text{trial}}}{2G \Delta t^k} \left[1 - \min \left\{ 1, \frac{\sigma_y}{\bar{\sigma}_0^{\text{trial}}} \right\} \right]. \quad (45)$$

4. Numerical examples

In this section, the mesh convergence of the proposed model will be demonstrated with different structured and unstructured meshes, and two numerical simulations will be performed to validate the proposed model against experiments. The 45 steel impact experiment is studied firstly; then in the simulation of Kalthoff test, the crack patterns under different impact velocities are considered.

Moreover, a study on the Taylor–Quinney coefficient is performed. The physical meaning of the Taylor–Quinney coefficient $\chi \in [0, 1]$ is the fraction of the inelastic work converted to heat. In most of existing work, this coefficient is set to be 0.9. However, Rittel et al. [47] recently found that this coefficient varied under different loading modes and for different materials. Therefore, the effect of χ is studied as follows. In the sequel, the cases with $\chi = 0, 0.5, 0.7$, and 0.8 will be examined. The extreme value $\chi = 0$ and an intermediate value $\chi = 0.5$ are studied to consider the extreme and special cases. Besides, based on the observation of Rittel et al. [47] on 1020 steel, the Taylor–Quinney coefficient varies between 0.7 and 0.9. Therefore, the cases with $\chi = 0.7$ and $\chi = 0.8$ are also looked into.

Besides, global sensitivity analysis is carried out for the impact experiment of two plates. The effect of three parameters g_c^{vol} , g_c^{dev} , and χ on a couple of key quantities is analyzed in detail.

Table 1
Material properties and parameters in 45 steel impact simulation.

Parameter	Symbol	Value	Unit	Source of data
Young's modulus	E	200	GPa	[24]
Poisson's ratio	ν	0.3	–	[24]
Mass density	ρ	7830	kg/m ³	[24]
Critical energy release rate for volumetric loading	g_c^{vol}	0.88	N/mm	–
Critical energy release rate for shear loading	g_c^{dev}	22	N/mm	[24]
Johnson-Cook parameter	A	496	MPa	[49]
Johnson-Cook parameter	B	434	MPa	[49]
Johnson-Cook parameter	C	0.07	–	[49]
Johnson-Cook parameter	N	0.307	–	[49]
Johnson-Cook parameter	m	0.804	–	[49]
Initial temperature	T_0	300	K	[49]
Melt temperature	T_m	1765	K	[49]
Courant number	CFL	0.1	–	–
Initial velocity	v_0	503	m/s	[49]
Mie-Grüneison equation of state parameter	C_{MG}	4.28×10^3	m/s	[42]
Mie-Grüneison equation of state parameter	S_1	1.275	–	[42]
Mie-Grüneison equation of state parameter	γ_0	1.68	–	[42]
Artificial viscosity parameter	b_1	0.06	–	[42]
Artificial viscosity parameter	b_2	1.5	–	[42]
Hourglass viscosity parameter	ε	0.1	–	[42]
Taylor-Quinney fraction	χ	0.9	–	[24]



Fig. 2. The geometry and initial conditions of 45 steel impact experiment from Li et al. [49]. The left plate impacts the right plate with velocity v_0 .

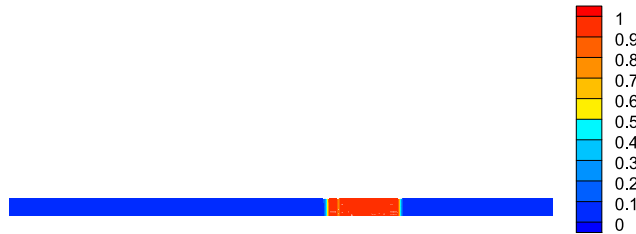


Fig. 3. The phase field profile under the deformed configuration.

4.1. The impact experiment of two plates

In this section, we will simulate the 45 steel impact experiment conducted by Hu et al. [48]. We adopt the same geometry, initial conditions, and boundary conditions as in the experiment and material parameters from Li et al. [49] listed in Table 1.

Consider an infinite plate with thickness $L_2 = 3.993$ mm is collided by another infinite plate parallel to it with thickness $L_1 = 1.996$ mm, and the impact is completely inelastic. The geometry and initial configuration are shown in Fig. 2. The initial velocity of the left plate (shown in brown) is 503 m/s, and the right plate (shown in green) is initially at rest. The whole geometry is totally traction free.

We use two meshes to study the effect of ℓ . In mesh 1, we use 20×600 structured quadrilateral elements whose initial edge length $h_1 = 0.01$ mm with phase field regularization parameter $\ell_1 = 0.02$ mm. In mesh 2, 40×1200 structured quadrilateral elements is used whose initial edge length $h_2 = 0.005$ mm with $\ell_2 = 0.01$ mm. Note that $\ell/h = 2$ for both setups.

The phase field profile in the deformed configuration is shown in Fig. 3, and the result is consistent with the observation by Hu et al. [48]. Fig. 4 shows the evolution of the velocity of the midpoint of the right end surface obtained from the experiment and from the simulation results with both meshes. It can be seen that the simulations with different meshes converge to nearly the same result, and the simulation results with mesh 1 and mesh 2 are both in good agreement with the experimental result, which validates the proposed phase field model.

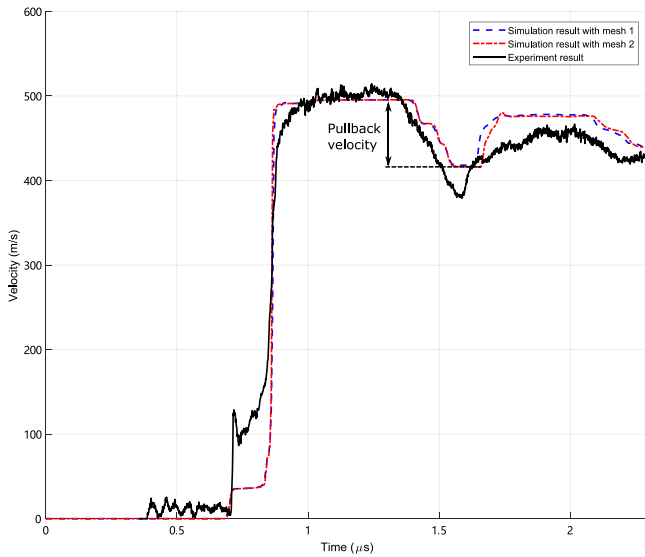


Fig. 4. The velocity of the right end surface by experiment conducted by Hu et al. [48] and simulations with mesh 1 and mesh 2.

Sensitivity analysis. Sensitivity analysis has been widely used to quantify the effect of uncertain input variables on the results of physical models, e.g., [50,51]. Here, the sensitivity of the results due to the uncertainty of three input parameters is analyzed in detail.

For the impact experiment of two plates, we have chosen the pullback velocity v_p of the right end surface and the crack location as output quantities. The pullback velocity is defined as the difference between the maximum velocity and the first minimum velocity in the history of the right end surface, as shown in Fig. 4. The crack location is where the phase field first reaches 0.999. As uncertainty parameters, g_c^{vol} , g_c^{dev} , and χ are selected. The dependence of variances of outputs on those of the input parameters will be estimated in the sequel. The detailed setup and the surrogate model for the sensitivity analysis is given in the Appendix.

For the sensitivity analysis, the commonly used variance-based Sobol' method [52] is employed. The meanings of the Sobol' indices are as follows. The first-order Sobol' index S_i , also known as the main effect, represents the fractional contribution of the uncertainty of the i th input parameter to the variance of the results. The second-order Sobol' index S_{ij} , $i \neq j$, measures the joint effect of the i th and j th input parameters on the variation of the results. The total Sobol' index S_i^{Tot} expresses the total effect of the variance of the results related to the i th input parameter, including its own sensitivity and that of all its interactions with the other variables.

The first order, second order, and total Sobol' indices for the pullback velocity and the crack location are shown in Figs. 5, 6, 7, 8, 9, and 10, respectively. Overall speaking, among individual parameters, χ affects the pullback velocity the most, about 95.35%, and g_c^{vol} affects the crack location the most significantly, about 72.74%; among parameter combinations, almost none has a joint effect on the pullback velocity, and $(g_c^{\text{vol}}, g_c^{\text{dev}})$ influences the crack location mostly, about 13.78%.

The effect of χ . As we have seen, χ has a significant effect on the result. Hence, the effect of χ is further studied. With mesh 1, the impact of two plates are simulated with $\chi = 0, 0.5, 0.7$, and 0.8 , and the velocity of the right end surface in each case is shown in Fig. 11, along with the experimental results in Hu et al. [48]. From the figure, we see that the results with different χ 's are nearly the same prior to $1.6 \mu\text{s}$ after the meeting of the two reflection waves at about $1.32 \mu\text{s}$, and the velocity of the free surface begins increasing again. After $1.6 \mu\text{s}$, the curve with $\chi = 0$ severely deviates from the experimental curve, and the result is totally off. On the other hand, the results with $\chi = 0.7, 0.8$, and 0.9 are quite similar. Besides, the case with $\chi = 0.5$ is the closest to the experimental result soon after $1.6 \mu\text{s}$, then it converges to the cases with $\chi = 0.7, 0.8$, and 0.9 .

4.2. The Kalthoff impact test

We next will study the Kalthoff impact test with different impact velocities and meshes. The Kalthoff impact experiment was firstly studied by Kalthoff [53,54], then by Zhou et al. [55,56]. The experimental results show that, when the impact velocity is less than a critical value, the crack propagates as a tensile crack with a long failure path, and the angle between the crack and loading direction is about 70° . When the impact velocity is greater than the critical value, the crack propagates as adiabatic shear bands with a short failure path, and the crack path direction is nearly the same as the loading direction.

Here, we will simulate the Kalthoff impact experiment under the impact velocities $v_0 = 10 \text{ m/s}$ and $v_0 = 40 \text{ m/s}$, respectively. The geometry and load configuration are shown in Fig. 12.

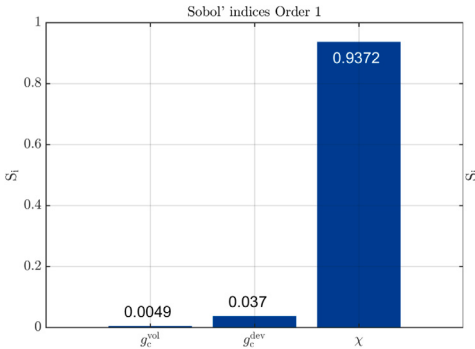


Fig. 5. The first order Sobol' indices for pullback velocity.

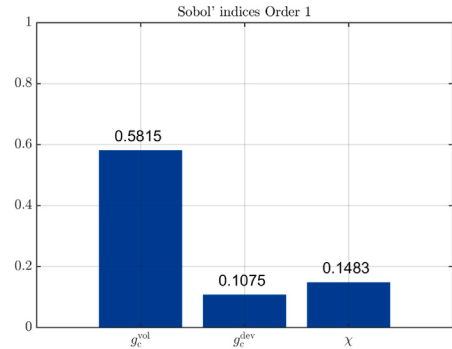


Fig. 6. The first order Sobol' indices for crack location.

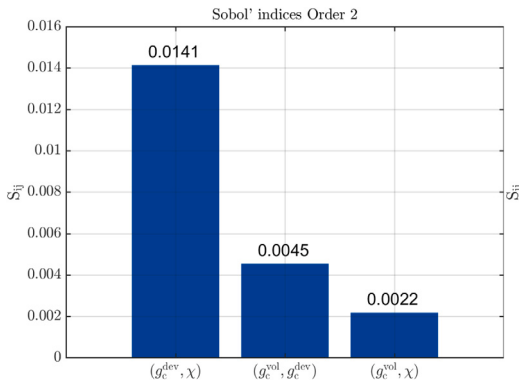


Fig. 7. The second order Sobol' indices for pullback velocity.

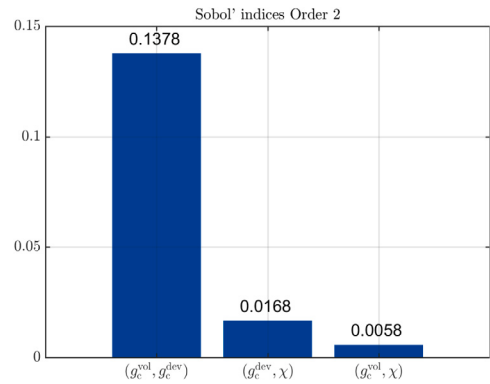


Fig. 8. The second order Sobol' indices for crack location.

The material properties and relevant parameters are the same as in Table 1. We use 38,494 unstructured quadrilateral elements whose minimal mesh size is about 0.05 mm and 76,180 unstructured quadrilateral elements whose minimal mesh size is about 0.01 mm as mesh 3 and mesh 4, respectively, and we adopt the phase field regularization parameter $\ell = 0.1$ mm as a constant.

The solution of equivalent plastic strain and phase field under impact velocity $v_0 = 10$ m/s by mesh 3 are shown in Fig. 13. From the results and by examining the driving forces, we confirm that the fracture mode is tensile fracture, and the angle between the fracture direction and loading direction is about 70°, which is consistent with experimental observation.

Fig. 14 shows the equivalent plastic strain and phase field under impact velocity $v_0 = 40$ m/s by mesh 3. From the results, we can see the fracture mode is shear banding, and the crack propagates along the loading direction. Besides, the crack length is much smaller than the tensile crack, which agrees with experimental observation.

The equivalent plastic strain field and phase field under impact velocity $v_0 = 10$ m/s by mesh 4 are plotted in Fig. 15. From the results, we can see that the fracture mode and crack path are the same as the results under mesh 3, which suggests that both simulations converge to the same result.

Fig. 16 shows the equivalent plastic strain and phase field under impact velocity $v_0 = 40$ m/s by mesh 4. From the results, we can see the fracture mode is still shear band, and the results are very similar with Fig. 14, which illustrates that both simulations converge to the same result again.

The effect of χ . The extreme case with $\chi = 0$ is examined first, in which case all the plastic energy is available for driving cracks, and there is no energy converted to heat. As is shown in Fig. 17, there is no apparent tensile crack under the impact velocity 10 m/s, which is not consistent with the observation of the experiment. Besides, there is abnormal crack tendency towards the lower left corner below the pre-existing crack under the impact velocity 40 m/s.

Then, the intermediate value with $\chi = 0.5$ is studied. As shown in Fig. 18, there is still no tensile crack under the velocity 10 m/s, but the abnormal crack tendency is slighter than that in Fig. 17 under the impact velocity 40 m/s.

Figs. 19 and 20 show the results of $\chi = 0.7$ and $\chi = 0.8$, respectively. From the results, we see that these two cases are very similar, and the tensile crack and shear bands are produced as before.

From the above results, we see that χ plays a very important role in the simulation of impact, and different χ 's lead to different crack paths.

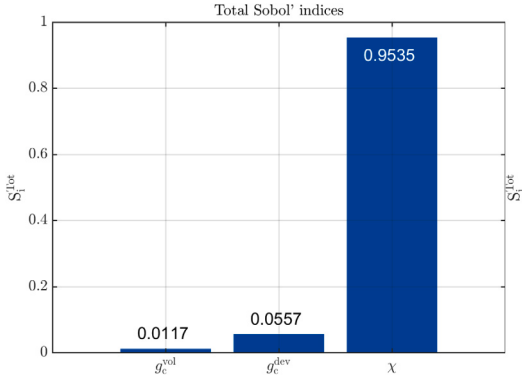


Fig. 9. The total Sobol' indices for pullback velocity.

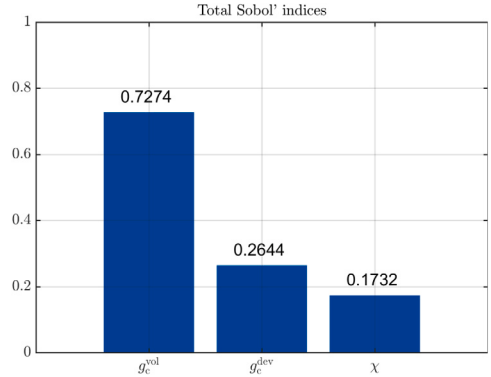
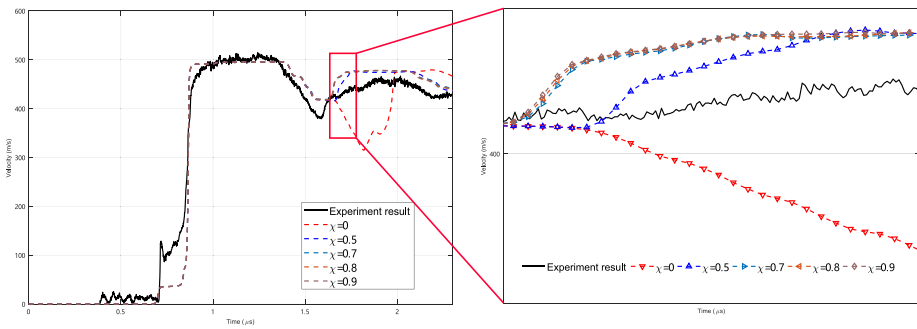
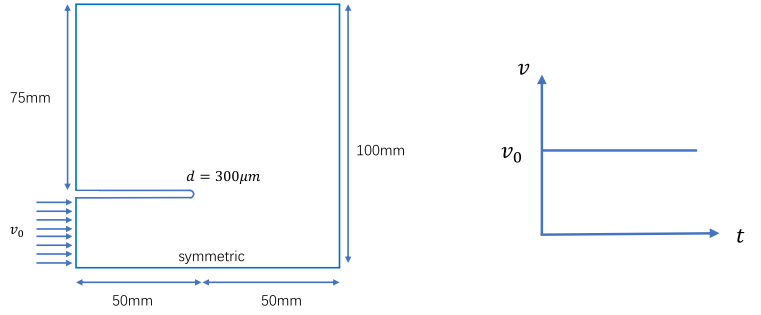


Fig. 10. The total Sobol' indices for crack location.

Fig. 11. The velocity of the right end surface by experiment and different χ .

(a) The geometry and boundary condition

(b) The loading configuration

Fig. 12. The Kalthoff test configuration.

5. Conclusions

In this paper, a phase field model is proposed based on the elastoplastic fluid framework for impact problems. The model is implemented based on a hydrodynamic code, which possesses a few features. First, the kinematics is handled in a fluid-style. This includes the Mie–Grüneisen equation of state and artificial viscosity introduced to account for the intense shock waves generated by impact, a typical fluid-style treatment distinct from most existing phase field models. Second, the elliptic operator for the phase field accounts for the difference between the current and the initial configurations, leading to the appearance of the Jacobian and the left Cauchy–Green tensor in the governing equation. Third, a new formulation for the thermodynamic driving force without artificial parameters for the phase field is developed to consider the different behaviors under volumetric and shear loadings based on the updated Lagrangian framework. Moreover, the Johnson–Cook model is adopted to incorporate the strain hardening, strain rate hardening, and thermal softening at finite strain and high strain rates. The proposed model converges to the same result under different meshes, and is validated by two experiments with excellent agreements. Besides, the effect of the Taylor–Quinney

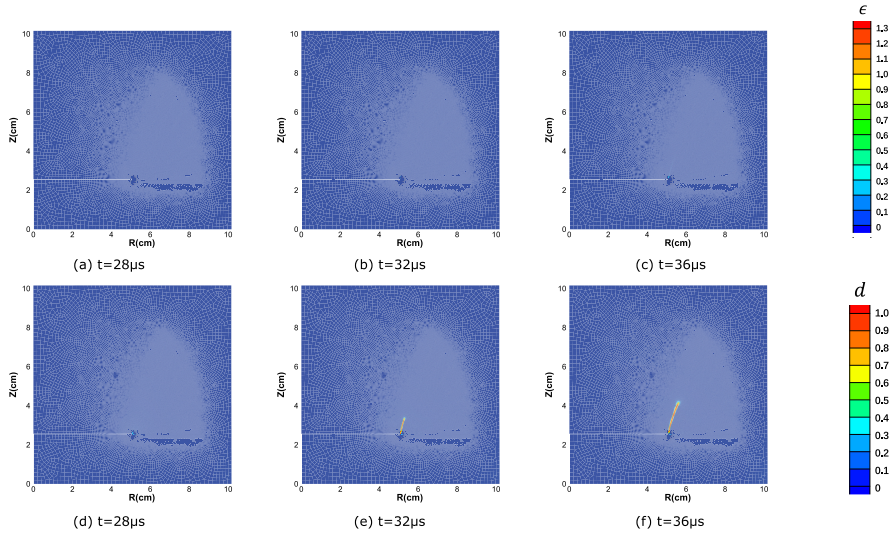


Fig. 13. The equivalent plastic strain and phase field at different times under the impact velocity $v = 10 \text{ m/s}$ by mesh 3.

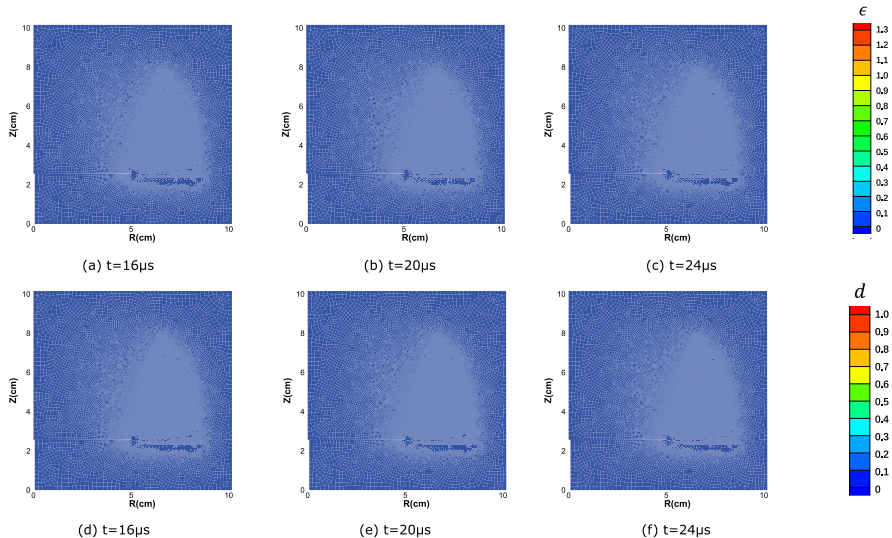


Fig. 14. The equivalent plastic strain and phase field at different times under the impact velocity $v = 40 \text{ m/s}$ by mesh 3.

coefficient is studied in detail, and systematic global sensitivity analysis is performed for the numerical experiment of the impact of two plates.

Declaration of competing interest

The authors declare that they have no known competing financial interests or personal relationships that could have appeared to influence the work reported in this paper.

Acknowledgments

This work is supported by the Science Challenge Project, China, No. TZ2016002, and by the National Natural Science Foundation of China, No. 12072043.